

Nature and Nurture? Comparing Ly α Detections in UV Bright and Fainter [O III]+H β Emitters at $z \sim 8$ With Keck/MOSFIRE

GUIDO ROBERTS-BORSANI ,¹ TOMMASO TREU ,¹ CHARLOTTE MASON ,^{2,3} RICHARD S. ELLIS ,⁴
 NICOLAS LAPORTE ,^{5,6} THOMAS SCHMIDT ,¹ MARUSA BRADAC ,⁷ ADRIANO FONTANA ,⁸ TAKAHIRO MORISHITA ,⁹
 AND PAOLA SANTINI 

¹Department of Physics and Astronomy, University of California, Los Angeles, 430 Portola Plaza, Los Angeles, CA 90095, USA

²Cosmic Dawn Center (DAWN)

³Niels Bohr Institute, University of Copenhagen, Jagtvej 128, 2200 København N, Denmark

⁴Department of Physics and Astronomy, University College London, Gower Street, London WC1E 6BT, UK

⁵Kavli Institute for Cosmology, University of Cambridge, Madingley Road, Cambridge CB3 0HA, UK

⁶Cavendish Laboratory, University of Cambridge, 19 JJ Thomson Avenue, Cambridge CB3 0HE, UK

⁷University of Ljubljana, Department of Mathematics and Physics, Jadranska ulica 19, SI-1000 Ljubljana, Slovenia

⁸INAF Osservatorio Astronomico di Roma, Via Frascati 33, 00078 Monteporzio Catone, Rome, Italy

⁹Infrared Processing and Analysis Center, Caltech, 1200 E. California Blvd., Pasadena, CA 91125, USA

ABSTRACT

The 100% detection rate of Ly α in a sample of four luminous $z \sim 8$ galaxies with red *Spitzer*/IRAC colors suggested objects with unusual ionizing capabilities and the presence of early (re)ionized bubbles in a neutral era. Whether such bubbles are a reflection of enhanced ionizing properties (nature) or an overdense environment (nurture), however, remains an open question. Here we aim to distinguish between these hypotheses with a spectroscopic search for Ly α in five fainter galaxies from the CANDELS-GOODS fields with Keck/MOSFIRE, selected on a similar IRAC excess and UV magnitudes that reflect reduced clustering effects. We detect $> 4\sigma$ line emission in only two targets, placing them at redshifts of $z_{\text{Ly}\alpha} = 7.1081$ and $z_{\text{Ly}\alpha} = 7.9622$, with rest-frame EWs of 16-17 Å that are $\sim 1.5 \times$ weaker than those of their bright counterparts. Comparing line detections we find a reduced rate of Ly α emission of $0.40^{+0.30}_{-0.25}$ in the faint sample compared to $1.00^{+0.00}_{-0.44}$ for the bright sample. The lower rate of the faint sample is well-matched by the predicted number of detections derived from simulations of a mostly neutral IGM and an intrinsic $\text{EW}_{0,\text{Ly}\alpha}$ distribution from $z \sim 6$ galaxies. However, even with an extreme EW model, it is challenging to match the detection rate of the luminous objects. SED-fitting of the faint galaxies indicates generally young, metal- and dust-poor systems, albeit with reduced star-forming properties compared to their luminous counterparts. We argue the enhanced detection rate in UV bright galaxies is likely a byproduct of both extreme ionizing properties as well as environment, where nature and nurture both play an important role. Ultimately, UV emission lines and direct measurements of clustering with *JWST* are required to resolve the physical nature of this puzzling population.

Keywords: galaxies: high-redshift, galaxies: ISM, galaxies: star formation, cosmology: dark ages, reionization, first stars

1. INTRODUCTION

Pinpointing the birth of the first stars and galaxies and determining their role in transforming the intergalactic medium (IGM) from a neutral state to com-

pletely ionized remains one of the holy grails of observational cosmology and one of the main motivations for next generation telescopes (e.g., the *James Webb* Space Telescope, Square Kilometre Array, and optical/IR Extremely Large Telescopes). A popular view is that reionization was driven largely by the abundant population of faint galaxies dominating the faint end of the galaxy luminosity function (Robertson et al. 2015; Robertson

2021). However, the rapid change in the ionization state of the IGM at redshifts $6 \lesssim z \lesssim 8$ (Mason et al. 2019b; Qin et al. 2021), may suggest that rarer, more luminous sources provided a dominant contribution in concluding the process (e.g., Naidu et al. 2020). While the high neutral fraction of the IGM beyond $z \simeq 8$ is well established (Treu et al. 2013; Mason et al. 2019b; Hoag et al. 2019; Bolan et al. 2021), constraints on the sources that governed the reionization process are still sorely lacking: are their properties similar to those of galaxies found at $z \lesssim 7.5$ or do they differ, perhaps reflecting an alternate evolutionary pathway as one approaches the first galaxies (e.g., Oesch et al. 2014; McLeod et al. 2016; Oesch et al. 2018)?

An important clue comes from spectroscopic observations of luminous galaxies with red *Spitzer* Space Telescope IRAC 3.6-4.5 μm colors - a so-called “IRAC excess”, generally attributed to intense [O III]+H β line emission polluting the IRAC 4.5 μm band. With rest-frame equivalent widths of $\text{EW}_0 \gtrsim 1500 \text{ \AA}$, such line emission is suggestive of extreme sources with intense radiation fields, resulting in unusually high fractions of Ly α detections at $z \gtrsim 7.5$ (Oesch et al. 2015; Zitrin et al. 2015; Roberts-Borsani et al. 2016; Laporte et al. 2017b,a; Stark et al. 2017; Hashimoto et al. 2018; Endsley et al. 2021; Laporte et al. 2021) in contrast with the much lower detection rates in magnitude-limited samples (c.f. Fontana et al. 2010; Pentericci et al. 2011; Schenker et al. 2014; Mason et al. 2018b, 2019b; Hoag et al. 2019). Perhaps the most marked example was the recent spectroscopic follow up of a sample of four luminous ($H_{160} \sim 25 \text{ AB}$; $M_{\text{UV}} \sim -22 \text{ mag}$), IRAC-excess galaxies selected by Roberts-Borsani et al. (2016, henceforth RB16) in the CANDELS fields, which revealed Ly α emission in each of the four objects with Keck/MOSFIRE and VLT/X-Shooter spectroscopy (RB16; Stark et al. 2017; Laporte et al. 2017a). The surprising 100% detection rate of the line is strong evidence for early ionized bubbles in a predominantly neutral medium.

Given the especially luminous nature of the sources, whether these bubbles are the consequence of extreme ionizing properties (i.e., nature) and/or due to clustered environments typical of more massive galaxies (i.e., nurture) remains an open question. As an example of the former, additional spectroscopy of these and similar sources revealed line emission from high-excitation UV lines (e.g., N V $\lambda 1240$, [C III], C III] $\lambda\lambda 1907, 1909$, and He II $\lambda 1640$) suggestive of hard spectra, extreme radiation fields (Stark et al. 2017) and possible non-thermal contributions (Laporte et al. 2017a; Mainali et al. 2018). The detection of these lines suggests this particular pop-

ulation of galaxies may harbor unusual properties and stellar populations that are able to more efficiently carve out large, early ionized bubbles and have enhanced Ly α production.

However, environmental effects likely also play a role. With three of the four luminous RB16 galaxies residing in the same CANDELS-EGS field, cosmic variance and a clustered environment may play a significant role: indeed, spectroscopic confirmations of fainter $z \simeq 7 - 9$ satellite galaxies around two of the RB16 EGS objects indicates the likely presence of overdensities, with physical separations between the galaxies extending merely 0.7-3.5 physical Mpc (pMpc) along the line of sight (Tilvi et al. 2020; Larson et al. 2022). Furthermore, the recent photometric analysis by Leonova et al. (2021) using deep *HST* Y-band and *Spitzer*/IRAC imaging revealed an enhancement of neighbouring galaxies around each of the three UV-bright EGS galaxies of the RB16 sample, by a factor of $\sim 3 - 9 \times$ compared to blank fields. Such analyses suggest a ubiquity of overdense regions around luminous, Ly α -emitting IRAC-excess sources, although deep spectroscopic measurements are required for confirmation.

Thus, recent analyses have revealed evidence for both exceptional properties and clustered environments for these intriguing samples, making it challenging to discern the primary cause of the early ionized bubbles. One way to disentangle the effects of nature (intrinsic properties) and nurture (environment) is to extend such analyses to fainter galaxies that are less subject to the same clustering effects expected in predominantly luminous samples (Barone-Nugent et al. 2014; Qiu et al. 2018; Harikane et al. 2022; Qin et al. 2022). As such, in this paper we aim to determine whether the fainter-end of the IRAC-excess galaxy population harbor similar intrinsic ionizing capabilities to their luminous counterparts. We therefore present the spectroscopic search for Ly α in five fainter ($M_{\text{UV}} \sim -21 \text{ mag}$) IRAC-excess sources with Keck/MOSFIRE, selected as part of the extended RB16 sample with identical data sets and thus minimizing selection effects and ideally suited for a one-to-one comparison with their luminous ($M_{\text{UV}} \sim -22 \text{ mag}$) counterparts.

The paper is structured as follows. In Section 2 we describe the target selection and photometric data sets adopted, Section 3 describes our Keck/MOSFIRE observations and presents the results of those observations. Section 4 compares the detection rates of Ly α across bright and fainter samples with Ly α -IGM modelling, while Section 5 derives and contrasts their intrinsic properties via SED-fitting. Finally, we present a summary and our conclusions in Section 6. Where relevant, we as-

sume $H_0 = 70$ km/s/Mpc, $\Omega_m = 0.3$, and $\Omega_\Lambda = 0.7$. All magnitudes are in the AB system (Oke & Gunn 1983).

2. TARGET SELECTION & PHOTOMETRY

To compare Ly α visibility statistics with the primary, luminous IRAC-excess sample of RB16 galaxies, we select a subset of the fainter galaxies presented in Table 5 of the same paper, which were selected in identical fashion to the bright sample - i.e., through an initial NIR color cut to constrain the location of the Lyman break, followed by photo- z modelling with EAzY (see RB16 for details) - albeit with fainter magnitude limits. A total of 5 galaxies were selected here (GSWY-2249353259, GSDY-2209651370, GNDY-7048017191, GNWY-7379420231, and GNWZ-7455218088) based on their approximate M_{UV} values and visibility with the Keck telescopes. Three of the targets reside in the GOODS-North field, two in the GOODS-South field and all have $H_{160} \geq 26.1$, $[3.6]-[4.5] \geq 0.5$ and reported photometric redshifts of $z_{\text{phot}} > 7$ from EAzY. Each of the targets benefit from deep *HST* and *Spitzer*/IRAC photometry, which we adopt from Bouwens et al. (2015): the filters included as part of the data set are optical filters from *HST*/ACS (F435W, F606W, F775W, F814W, F850LP), NIR filters from *HST*/WFC3 (F098M, F105W, F125W, F140W, F160W) and IR filters from *Spitzer*/IRAC (CH1 and CH2) - for details on the construction of the data set and RB16 selection, we refer the reader to Bouwens et al. (2015) and RB16.

We fit all of the available photometry for each object using the Bayesian Analysis of Galaxies for Physical Inference and Parameter EStimation (Bagpipes; Carnall et al. 2018) SED-fitting code, adopting a composite star formation history model consisting of a smooth, delayed component as well as a current burst of star formation defined by a delta function. The choice of model is primarily motivated by previous studies highlighting the need for both a smooth component to trace the bulk of the stellar mass formed, as well as a more recent burst to account for intense and shorter-duration star formation that boosts [O III]+H β nebular line emission in the *Spitzer*/IRAC bands (e.g., Stark et al. 2017; Roberts-Borsani et al. 2020; Laporte et al. 2021). Additionally, the model and parameter ranges are virtually identical to those adopted by Stark et al. (2017) for characterization of the luminous RB16 IRAC-excess objects and thus allows for a close comparison of results. The free parameters of the delayed component and adopted ranges were a stellar mass ($\log M_*/M_\odot$) of [6,12], star formation timescale (τ) of [0,30] Gyrs, and metallicity (Z/Z_\odot) of [0,2]. For the burst component, we allow a stellar

mass of $\log M_*/M_\odot$ =[6,12] and link the metallicity to that of the delayed component. Additionally, we assume the galaxy system has a dust content (A_{v} /mag) of [0,2], an ionization parameter ($\log U$) of [-4, -1] and a velocity dispersion for all absorption and emission lines of 150 km s $^{-1}$. Redshifts are allowed to vary between $z = [0,15]$. The resulting photo- z distributions and SEDs are plotted in Figure 1, where we find the photometric redshift solutions are virtually identical (and within errors) to those reported in Table 5 of RB16. We summarize the list of targets, along with their basic photometric quantities, in Table 1.

For comparison, we compile the photometric properties of the luminous RB16 sample in the bottom half of Table 1. Our faint sample has a mean H_{160} magnitude of 26.22 ± 0.15 AB and absolute magnitude (assuming photometric redshifts and a UV slope of $\beta = -2$) of -20.93 ± 0.15 mag, compared to 25.12 ± 0.06 and -22.02 ± 0.06 (assuming spectroscopic redshifts) for the bright sample. Adopting the $M_{\text{UV}} - M_h$ relation (where M_h denotes the dark matter halo mass) from Mason et al. (2015), we estimate the $\Delta M_{\text{UV}} \sim 1$ mag difference to translate to the bright galaxies residing in halos $\sim 3 \times$ more massive than the fainter ones, and consistent with simulations showing $m_{\text{UV}} < 25.5$ AB galaxies residing in larger ionized bubbles (Qin et al. 2022).

3. KECK/MOSFIRE OBSERVATIONS

3.1. Y -band Spectroscopy

For our spectroscopic campaign, we used the Multi-Object Spectrometer for Infra-Red Exploration (MOSFIRE; McLean et al. 2012) on the Keck I telescope, targeting each of our sources with Y -band spectroscopy in search for Ly α emission. MOSFIRE slitmasks were constructed using the MOSFIRE Automatic GUI-based Mask Application (MAGMA) software and slit widths of 0.7" (affording a spectra resolution of $R \sim 3500$). Thanks to MOSFIRE's large FOV ($\sim 60' \times 30'$) the primary targets were multiplexed over a total of 2 slitmasks to increase observing efficiency - the primary targets included on Mask 1 were GSWY-2249353259 and GSDY-2209651370, while those included on Mask 2 were GNDY-7048017191, GNWY-7379420231 and GNWZ-7455218088. In both slitmasks, a bright nearby star was included in one of the slits for monitoring seeing and throughput purposes.

The observations were distributed over an approximate 7-month window and carried out over a total of 6 nights (5 full nights and 2 half nights; 24th November 2020, 25th November 2020, 7th December 2020, 20th April 2021, 21st April 2021, 16th May 2021 and 17th May 2021 - the latter two of which were half nights) us-

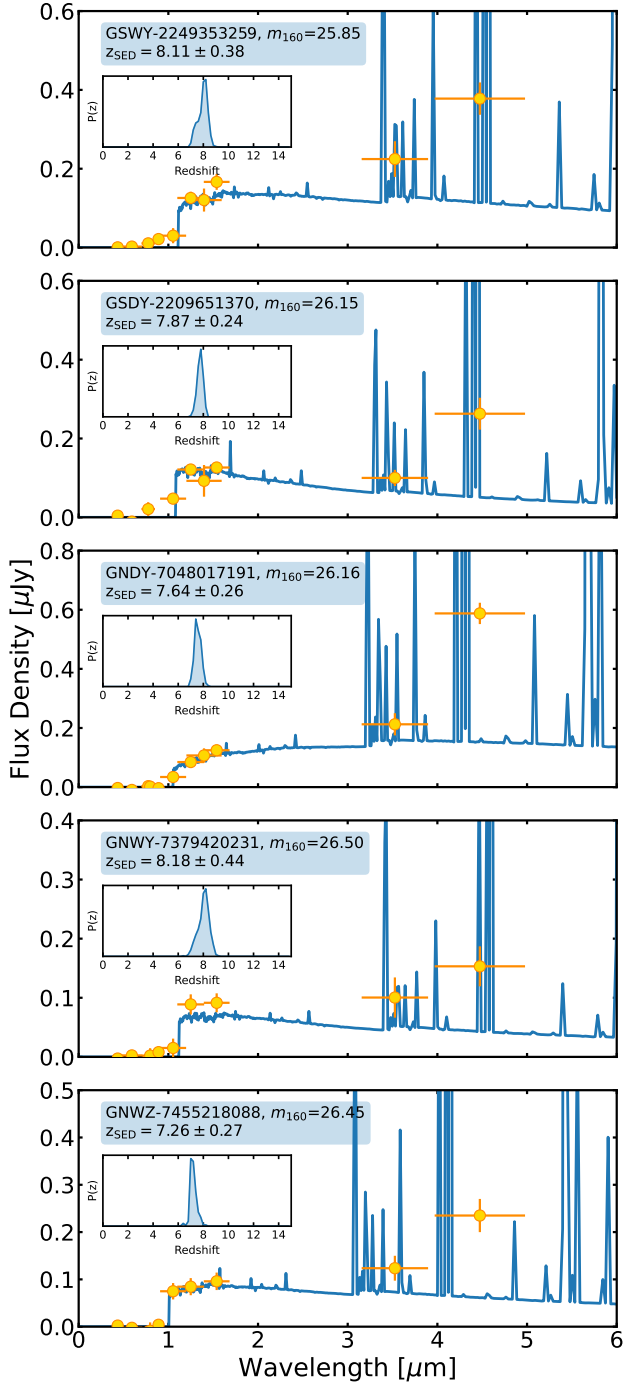


Figure 1. The best fit SEDs (blue lines) of our 5 primary targets, as well as their associated *HST* and *Spitzer*/IRAC photometry (orange points with 1σ uncertainties). The inset plot shows the photometric redshift distribution resulting from the fit.

ing a $1.25''$ ABBA dither pattern - the precise amplitude of the dither was carefully checked to ensure the primary sources did not fall on any slit-contaminating sources. While most of the first half of 24th November 2020 was lost due to poor weather conditions and the entire night of 20th April 2020 lost due to cloud coverage, the rest of the observations were carried out in good weather conditions and sub-arcsec seeing ($\sim 0.84''$, $\sim 0.87''$, $\sim 0.73''$, $\sim 0.63''$, $\sim 0.67''$ and $\sim 0.91''$ for 24th November 2020, 25th November 2020, 7th December 2020, 21st April 2021, 16th May 2021 and 17th May 2021, respectively). A summary of the targets and the telescope observations is provided in Table 1. In the case of Mask 1, it became apparent after the second night that the slit containing GSDY-2209651370 was too long ($\sim 3'$), causing some curvature of the resulting sky lines at the opposite end of the target’s position. As such, the slit was shortened to $\sim 1.9'$ to avoid the issue further.

The data were reduced using the `PypeIt` data reduction package (Prochaska et al. 2020; Prochaska et al. 2020), which uses telescope/instrument-specific data reduction scripts invoked from an input configuration file (henceforth referred to as the “`PypeIt` file”). The `PypeIt` file takes as input the science and calibration files to reduce, as well the parameters required to reduce, calibrate and co-add the data. We adopt the default Keck/MOSFIRE parameters ¹ and reduce the data in ABBA sequence blocks (i.e., for a given sequence, A-B and B-A subtraction is performed for background subtraction before co-adding both A frames and both B frames, resulting in two background-subtracted images), using the spectral trace of a bright star in one of the slits on each mask as a position reference. The co-added science exposures were used for wavelength calibration and tilt measurements, while flat frames were used for slit edge tracing in addition to flat-fielding. We note that in the case of Mask 1 (i.e., the GOODS-S targets), we used only the flats of 7th December 2020, since this allowed us to artificially define the slit traces of that night onto the data taken on 24th and 25th November 2020, thereby providing us with a significantly improved wavelength solution based on the smaller slit adopted for the December observations. The reduced A-B (or B-A) data frames were subsequently co-added using the extracted 1D spectra from each frame as weights, and flux-calibrated using a sensitivity function (i.e., the ratio of F_λ flux density to electron count density) generated from an archived, flux-calibrated standard star spectrum from ESO, providing us with fully reduced,

¹ https://pypeit.readthedocs.io/en/release/pypeit_par.html

calibrated and co-added 2D and 1D spectra which we display in Figure 2. The total exposure times resulting from the observations and data reduction were ~ 6.3 hours for the GOODS-S mask and ~ 11.8 hours for the GOODS-N mask.

3.2. *Detections of Ly α at $z > 7$*

Each of the resulting 1D and 2D Y -band spectra presented in Figure 2 were visually (and independently) inspected by two authors (GRB and NL) to search for Ly α emission. Emission lines were found in two of the targeted galaxies, namely GNWY-7379420231 and GSDY-2209651370, and are shown in Figure 3.

For GNWY-7379420231, a single, narrow emission line is clearly visible in the 2D spectrum, showing a positive, central component with two negative counterparts above and below it separated by approximately ± 14 pixels, which corresponds to our dither choice of $1.25''$. The line resides between sky lines and a simple Gaussian fit (ignoring potential line asymmetries due to a neutral IGM) finds the central wavelength to lie at 9859.5 Å with an integrated signal-to-noise ratio (SNR) of $\sim 4.5\sigma$. No other convincing emission line is seen in the rest of the 1D or 2D spectra. To ensure the line is not due to a spurious bad frame or artefact in the data, we statistically verify its robustness via the adoption of a Monte Carlo approach, where we randomly sample (without replacement) 50% of the entire data set and 2D co-added those selected spectra before re-estimating the SNR of the apparent line. Repeating this 100 times, we find that 59% of the iterations reveal a $> 3\sigma$ line, while this increases to 93% if we perform the same simulations with 75% of the data. With these statistics in mind, we conclude that the line is highly unlikely to result from spurious artefacts or a bad frame and is statistically robust. A similar case is found for GSDY-2209651370, which displays a single, broad emission line: the line itself falls behind a sky line, however it is sufficiently broad to be clearly visible either side of the sky line and a positive/negative trace pattern similar to the line in GNWY-7379420231 is seen at the expected positions. Again, no other line is found in the rest of the 1D or 2D spectra. Masking the sky line and fitting another simple Gaussian profile, we find the emission line has a central wavelength of 10898.0 Å and an integrated SNR of $\sim 6\sigma$. To ensure statistical robustness we perform the same test as done above for GNWY-7379420231 (always with the sky line masked) and find 66% and 97% of the iterations reveal a $> 3\sigma$ line for stacks of 50% and 75% of the data, respectively. As such, we also deem this line statistically significant.

Both of the identified lines are consistent with Ly α emission at $z > 7$ and the hypothesis of strong [O III]+H β emission lines as the cause of the especially red *Spitzer*/IRAC band (see [Roberts-Borsani et al. 2020](#) for a description of Balmer break contributions to the red colors at $z \gtrsim 7.5$, however). As such, we confirm GNWY-7379420231 and GSDY-2209651370 at redshifts of $z_{\text{Ly}\alpha} = 7.108$ and $z_{\text{Ly}\alpha} = 7.962$, respectively, consistent with their $P(z)$'s estimated with [Bagpipes](#).

Correcting for instrumental broadening with a Gaussian fit to a nearby sky line, we find the emission line of GNWY-7379420231 to be just unresolved ($\delta\sigma_{\text{gauss}} = 0.24$ Å) and thus assume a maximum FWHM given by the sky line. This is not the case for GSDY-2209651370, whose emission line is significantly wider. The instrumentally-corrected Gaussian fits to the lines yield peak fluxes of $4.7 \pm 1.6 \times 10^{-19}$ erg s $^{-1}$ cm $^{-2}$ Å $^{-1}$ and $2.0 \pm 0.5 \times 10^{-19}$ erg s $^{-1}$ cm $^{-2}$ Å $^{-1}$, integrated fluxes of $1.5 \pm 0.7 \times 10^{-18}$ erg s $^{-1}$ cm $^{-2}$ and $2.4 \pm 0.8 \times 10^{-18}$ erg s $^{-1}$ cm $^{-2}$, and line FWHMs of 3 ± 1 Å and 12 ± 3 Å (corresponding to $\Delta v_{\text{Ly}\alpha} = 99 \pm 32$ km s $^{-1}$ and $\Delta v_{\text{Ly}\alpha} = 340 \pm 79$ km s $^{-1}$) for GNWY-7379420231 and GSDY-2209651370, respectively. Assuming a flat, underlying continuum given by the H_{160} photometry, these would correspond to rest-frame equivalent widths of $\text{EW}_{0,\text{Ly}\alpha} = 16 \pm 8$ and $\text{EW}_{0,\text{Ly}\alpha} = 17 \pm 6$.

For non-detections of Ly α in GSWY-224935325, GNDY-7048017191, and GNWZ-7455218088, we place robust upper limits on the integrated flux and EW of the line. For the former, we take the median noise value in an uncontaminated (i.e., free of sky lines) portion of the noise spectrum, close to the photometric redshift of each galaxy and multiply the resulting value by the square-root of the number of pixels considered. For the latter, we use the resulting upper limit on the integrated flux and divide by the H_{160} continuum as well as a $(1+z_{\text{phot}})$ factor as above to obtain the upper limit on the rest-frame EW. We summarize these properties in Table 1.

4. COMPARING LYMAN- α DETECTION RATES WITH MODELS

Here we aim to place the detection rates found for the UV bright and fainter IRAC-excess samples into context: how do the rates compare, and how well (or poorly) are they matched to simulations of a neutral intergalactic medium and an assumed $\text{EW}_{0,\text{Ly}\alpha}$ distribution function? Quantifying the first of the two points determines whether any apparent differences are statistically significant, while the second determines whether our understanding of the $z \sim 8$ IGM and underlying physics of typical galaxy populations can explain the derived detection rates - the models account for cluster-

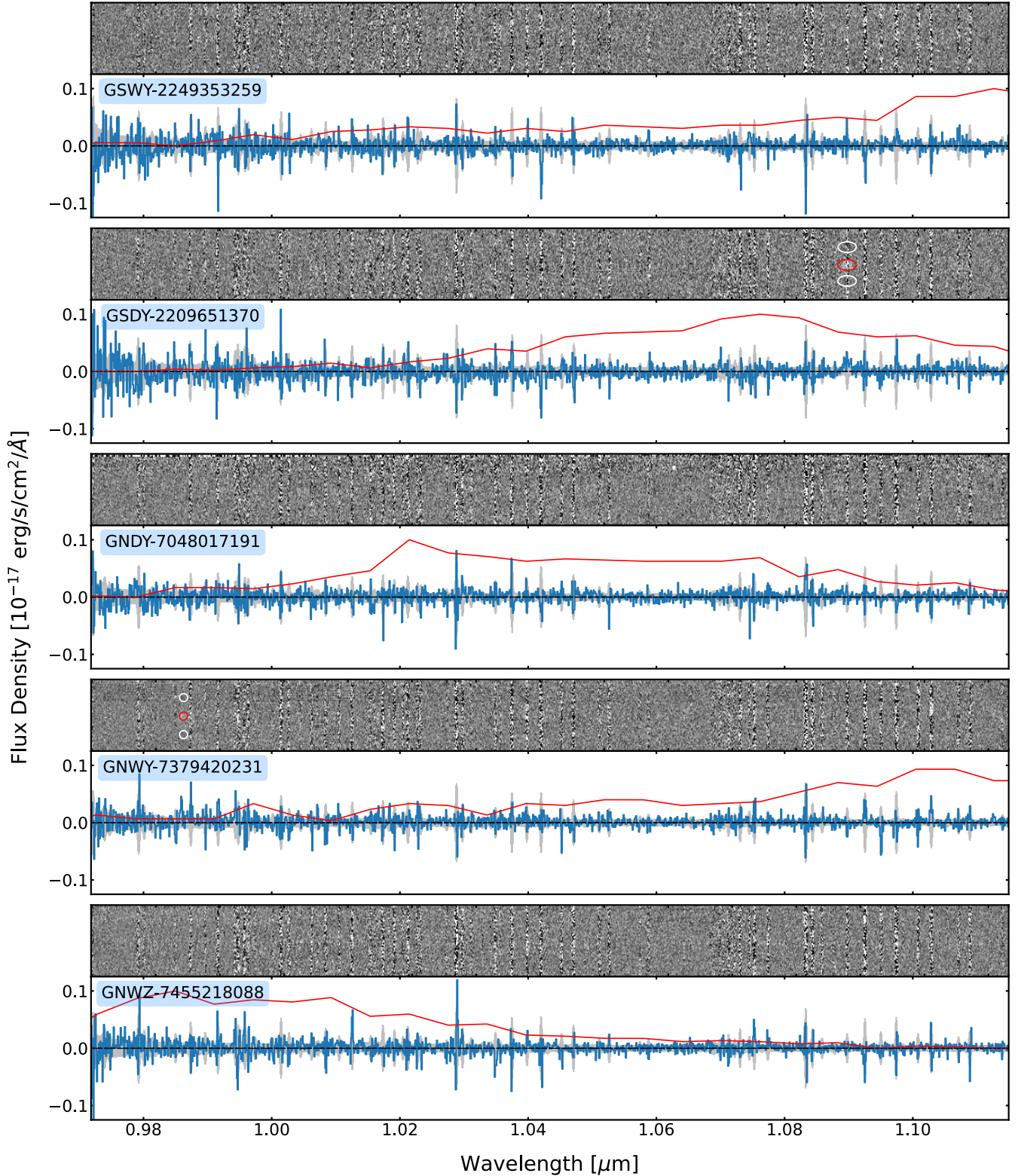


Figure 2. The 2D (top) and 1D (bottom) Keck/MOSFIRE spectra of each of our 5 targets in the GOODS-S and GOODS-N fields. Each of the spectra were reduced with the `TypeIt` data reduction software. In each case, red and white circles in the top panels mark the positive and negative traces of Ly α detections. Blue lines, grey-shaded regions, and redlines in the bottom panels denote the extracted 1D spectra, associated 1σ uncertainties, and the `Bagpipes`-derived Ly α redshift probability function, respectively.

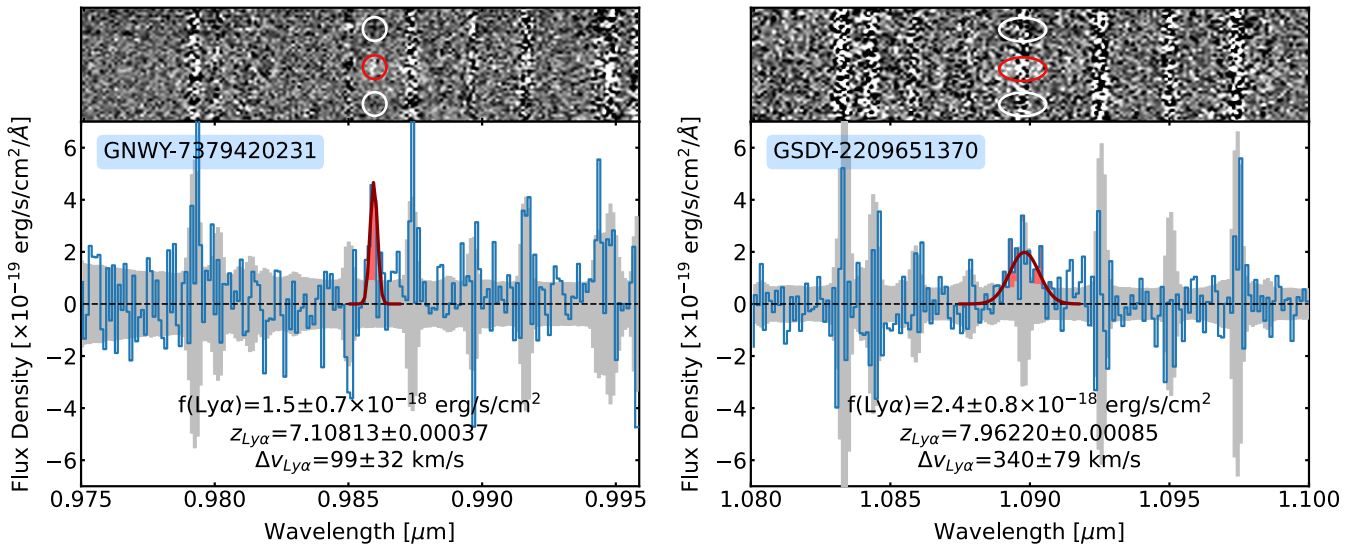


Figure 3. Ly α detections for two of our targeted galaxies: GNWY-7379420231 (left) and GSDY-2209651370 (right). Each 2D spectrum is shown in the top panel, with red and white circles to mark the positive and negative Ly α traces respectively, while the bottom panels show the collapsed 1D spectra (blue line), the associated 1σ uncertainty array (grey fill), and the best fit Gaussian model (dark red line) to each Ly α detection.

ing effects (i.e., the nurture effect), and thus allow us to quantify whether a change in the intrinsic properties of galaxies (i.e., the nature effect) is also needed.

For the first point, out of our five faint $z > 7$ IRAC-excess sources targeted with Keck/MOSFIRE, we find convincing Ly α detections in only two sources. Using the small number statistical limits presented by Gehrels (1986), this places the Ly α detection rate in our sample at $0.40^{+0.30}_{-0.25}$ (assuming 16% and 84% binomial percentiles). While the small number statistics prevent us from claiming statistically significant differences, the detection rate found here suggests differences with the $1.00^{+0.00}_{-0.44}$ detection rate of Ly α in the primary, luminous sample of RB16 determined by Stark et al. (2017). The low intensities, integrated line fluxes and small EWs of the detected lines also make these among the faintest and weakest Ly α emission found thus far: both of our line detections display rest-frame EWs of 16-17 Å, well below the Ly α emitter threshold of $\text{EW}_0 > 25$ Å generally assumed for inclusion as LBGs in reionization-constraining studies, and a median factor of $\sim 1.5 \times$ weaker than the EWs reported for their luminous IRAC-excess counterparts.

On the second point, the flux of Ly α we observe is the product of the intrinsic Ly α flux that emerges from the ISM and the fraction that is transmitted through the reionizing IGM. The transmitted fraction is thus a function of the integrated optical depth of Ly α through the IGM, determined by the distribution of neutral gas due to reionization, and the line shape of Ly α determined from radiative transfer of the line through the galaxy ISM. To interpret our observations we compare our Ly α detection rate to that expected from inhomogeneous reionization simulations using a Monte Carlo simulation. For each IRAC-selected galaxy we generate 1000 mock realizations of its Ly α EW and compare to the reported 1σ uncertainty (from Table 1) to classify the mock observations as a detection or not. The EWs are sampled from the model EW distributions by (Mason et al. 2018a,b) which are a function of UV magnitude and the IGM neutral fraction $p(W|M_{\text{UV}}, \bar{x}_{\text{HI}})$, constructed by forward-modelling an assumed intrinsic Ly α EW distribution through the realistic inhomogeneous reionization Evolution of Structure simulations over thousands of sightlines (Mesinger et al. 2016). In this way we account for the expected UV magnitude dependence of Ly α transmission during reionization, whereby the brightest galaxies live in overdensities that should reionize early and thus have higher Ly α transmission (e.g., Mason et al. 2018a,b; Qin et al. 2021; Leonova et al. 2021).

For each galaxy, we sample a UV magnitude, and redshift in the case of the non-detections, from within the 1σ uncertainties in Table 2 (see Section 5) and Table 1, respectively. We then sample the IGM neutral fraction at the spectroscopic or sampled photometric redshift from the model-independent constraints on the IGM timeline by Mason et al. (2019a), which conservatively includes only the Planck Collaboration et al. (2020) electron scattering optical depth and quasar dark pixel fraction (McGreer et al. 2015). For example, at $z \sim 8$ the inferred IGM neutral fraction is $\bar{x}_{\text{HI}} = 0.73^{+0.15}_{-0.27}$. We then sample from the corresponding Ly α EW distribution $p(W|M_{\text{UV}}, \bar{x}_{\text{HI}})$ by Mason et al. (2018a). Simulated EWs above the 2σ limit (we choose a 2σ threshold to mimic the lowest significance of the detected line EWs in Table 1) given the galaxy's observed EW uncertainty is classified as a detection. We repeat this process 1000 times for each galaxy to build a probability distribution for the expected number of detections.

In Figure 4 we show the results of these simulations. The left panel shows the probability distribution of the expected number of 2σ (EW) detections for the UV bright IRAC-selected sample by RB16, and the right panel shows the same for the fainter sample presented here. The grey shaded region shows the expected number of detections for the “normal” $p(W|M_{\text{UV}}, \bar{x}_{\text{HI}})$ EW distribution model by Mason et al. (2018a), which assumes an intrinsic Ly α EW distribution from an empirical model built using $-16 \lesssim M_{\text{UV}} \lesssim -21$ Lyman break galaxies, which were not selected by strong IRAC excesses (De Barros et al. 2017; Fuller et al. 2020; Bolan et al. 2021).

As discussed by Mason et al. (2018b) this intrinsic distribution fails to match the observed frequency of detections in the bright IRAC-excess galaxies, implying that these galaxies have enhanced Ly α emission compared to non-IRAC excess galaxies, or enhanced IGM transmission that is not accounted for in current simulations (as these galaxies are situated already in the most transmissive, early reionized regions in our simulations), or a combination of these factors. We thus also predict the expected number of detections for two additional intrinsic Ly α EW models. The first is an “extreme” model where these galaxies are given the intrinsic EW distribution for UV faint galaxies, which typically have higher EW at lower redshifts (this is identical to the “high EW” model by Mason et al. 2018b). The second is an EW distribution for $> L_{\star}$ galaxies at $z \sim 6$, including a number with strong IRAC-excesses, by Endsley et al. (2021) which may be more appropriate for our sample. We find the bright galaxies challenging to explain with any of our models. Only our “extreme”

EW model has some probability of all 4 galaxies being detected. We ran an additional simulation in a fully ionized universe and found that, even then, detecting Ly α in 4/4 UV bright galaxies was unlikely given our intrinsic EW models. On the other hand, we find that our fainter sample is consistent within 1σ with all three intrinsic EW models, and most consistent with the [Endsley et al. \(2021\)](#) distribution. Such a result suggests that these fainter IRAC-excess galaxies are fully consistent with current constraints on reionization, though their implied ionizing properties may favour enhanced Ly α emission compared to galaxies not selected with an IRAC excess (the “normal” model).

From our derived detection rate, measured line strengths, and Ly α simulations (which account for both intrinsic galaxy physics and clustering effects), we conclude that the brightest IRAC-excess galaxies likely transmit enhanced levels of Ly α due to both (i) very high intrinsic EWs ($\gtrsim 100$ Å) and (ii) residing in the most overdense, early reionized regions. Their fainter IRAC-selected counterparts, on the other hand, do not emit such strong Ly α , likely due to having less intense ionizing radiation fields (as discussed in the following section), and are consistent with models where they reside in less overdense environments ionized by $< L_*$ galaxies.

5. ARE BRIGHT AND FAINTER IRAC-EXCESS GALAXIES INTRINSICALLY DIFFERENT? CLUES FROM SED MODELLING

Quantifying the gaseous and stellar properties of our sample of fainter galaxies and comparing to those of the UV bright IRAC-excess galaxies allows us to assess whether the differences in their Ly α detection rates (quantified and discussed in Section 4) are attributable to differences in physical properties (i.e., nature). While we do not possess the additional J – and H –band MOSFIRE spectra used by e.g., [Stark et al. \(2017\)](#) and [Mainali et al. \(2018\)](#), or longer-wavelength NIR X-Shooter data by [Laporte et al. \(2017a\)](#), to constrain the radiation fields of the UV bright RB16 galaxies through detections (or upper limits) of N V, C IV, He II, and [C III] line emission, it is nevertheless instructive to determine and contrast their properties using the deep photometry available and new spectroscopic redshifts. We thus update the best-fit models for GNWY-7379420231 and GSDY-2209651370 by incorporating their spectroscopic redshifts and re-running **Bagpipes** as described in Section 2.

We find in all cases the photometry of our faint objects is well fit by the models and reveal underlying properties within expected ranges, with stellar mass values

of $\log M_*/M_\odot = [8.29, 9.17]$, star formation rate (SFR) values of $\log \text{SFR}/M_\odot \text{ yr}^{-1} = [0.28, 1.16]$, specific SFR values of $\log \text{sSFR}/\text{yr}^{-1} = [-8.01, -8.00]$, stellar ages of [285, 408] Myrs, metallicities of $Z/Z_\odot = [0.34, 1.40]$, dust contents of $A_V = [0.27, 1.24]$, and ionization parameters of $\log U = [-2.52, -1.48]$. We calculate absolute UV magnitudes and slopes directly from the best-fit SED – i.e., we adopt a bootstrap method where, for a sample of 1000 SEDs extracted using the posterior distributions of the **Bagpipes** free parameters, we fit the flux density between (rest-frame) wavelengths of 1300–2100 Å with a simple power law to measure β . Simultaneously, we measure M_{UV} assuming the flux density at 1600 Å and distance modulus given by the spectroscopic (or photometric) redshift. Such an approach results in UV slopes of $\beta = [-2.81, -1.60]$ and absolute UV magnitudes of $M_{\text{UV}} = [-22.13, -20.28]$.

Our reported values – shown in Table 2 – are consistent with those determined by [Stark et al. \(2017\)](#), see their Table 3) for EGS-zs8-1, EGS-zs8-2 and COS-zs7-1 (referred to as COSY here), in that they indicate more extreme systems than more representative samples of $z \sim 8$ galaxies (e.g., [Strait et al. 2020](#); [Roberts-Borsani et al. 2022](#)), with generally young stellar populations, low dust and metal contents, high ionization parameters, blue UV slopes, and elevated specific SFR values. Interestingly, however, in comparing to values found by [Stark et al. \(2017\)](#) we also observe some hints of a dichotomy between some properties of the bright and faint IRAC-excess samples. With ranges of $\log \text{sSFR}/\text{yr}^{-1} = [-8.14, -7.61]$, $Z/Z_\odot = [0.0016, 0.13]$ (assuming $Z_\odot = 0.02$), and $A_V/\text{mag} = [0.01, 0.02]$, the bright sample displays specific SFRs approximately $1.6\times$ larger than found here, lower metallicities by a factor of $\sim 0.1\times$, and reduced dust contents by a factor of $\sim 0.02\times$, all indicative of younger and more extreme star-forming systems that are likely to have boosted Ly α emission and enhanced ionizing capabilities to carve out early ionized bubbles. Although spectroscopic confirmations are required to confirm such interpretations (through emission line diagnostics and continuum measurements), the distinction in photometric properties found here suggests the physics of the two populations may differ and provide some explanation for the differing detection rates of Ly α . Upcoming and unprecedented observations (spectroscopic and photometric) with *JWST* (e.g., GO 1747, ERS 1324, ERS 1345, and GO 2279) will confirm these tantalizing clues by providing the rest-frame UV, optical, and IR diagnostics ([Roberts-Borsani et al. 2021](#)) required to disentangle intrinsic galaxy physics (nature) from environmental

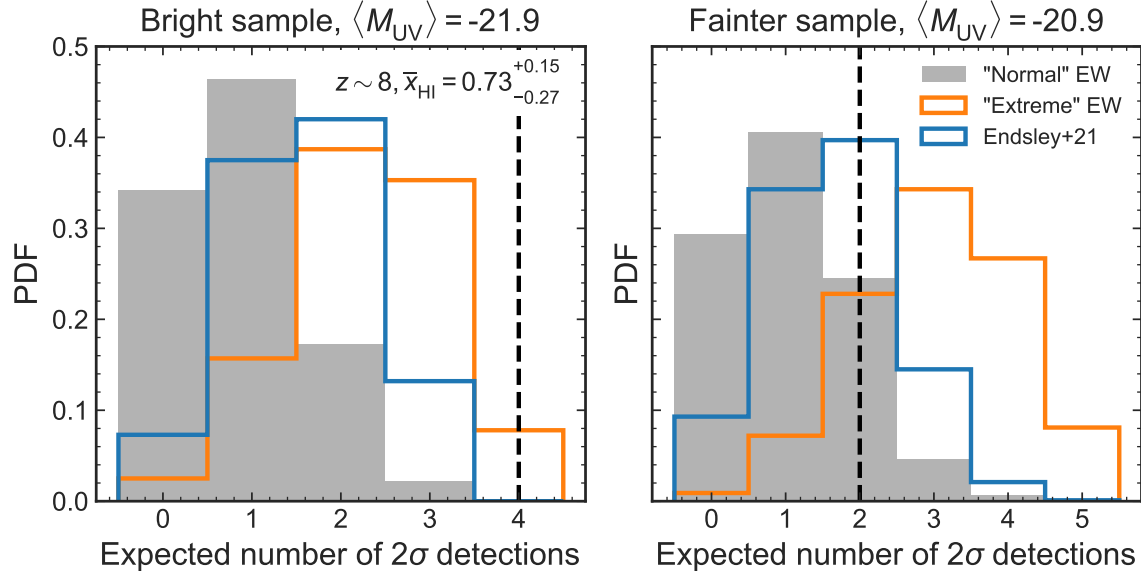


Figure 4. Probability distribution of expected number of 2σ Ly α detections for galaxies with the same observed photometric properties, redshifts and EW uncertainties as in Table 1, forward-modelled using inhomogeneous reionizing IGM simulations (Mason et al. 2018b). For each galaxy we sample the IGM neutral fraction at their spectroscopic redshift (or marginalize over photometric redshift) from the model-independent constraints on the reionization timeline by Mason et al. (2019a), which includes only the CMB electron scattering optical depth (Planck Collaboration et al. 2020) and the dark pixel fraction in the spectra of $z \gtrsim 5.5$ quasars (McGreer et al. 2015). We use three intrinsic Ly α EW distributions: “normal” (grey shaded region) – the standard model as a function of UV magnitude and IGM neutral fraction by Mason et al. (2018b), “extreme” (orange line) – identical to the “high EW” model by (Mason et al. 2018b), where these galaxies are given the same intrinsic EW distribution as $M_{\text{UV}} \sim -16$ galaxies, which typically have stronger emitted EWs; and the distribution observed by Endsley et al. (2021) for $1 - 6L_*$ galaxies at $z \sim 6$ (blue line). Black dashed lines show the observed number of $\geq 2\sigma$ detections. The number of detections in our fainter sample is consistent with all of our models for Ly α , however, the bright sample is challenging to explain without requiring these galaxies have very extreme intrinsic Ly α emission.

(nurture) effects and determine the primary cause of the early ionized bubbles.

6. SUMMARY & CONCLUSIONS

We present deep Keck/MOSFIRE spectroscopy over five sources in the GOODS fields, selected on account of their *Spitzer*/IRAC excesses, intrinsically fainter ($M_{\text{UV}} \sim -21$ mag) magnitudes to minimize clustering effects, and $z \sim 8$ photometric redshifts. We confirm two of our sources with $> 4\sigma$ Ly α emission at $z_{\text{Ly}\alpha} = 7.1081$ and $z_{\text{Ly}\alpha} = 7.9622$ and, through a comparison of Ly α detection rates, detailed simulations of IGM–Ly α opacity, and characterization of galaxy physics with SED-fitting, we offer a comparison between the ionizing capabilities of these faint galaxies and their more UV luminous counterparts. Our findings can be summarized as follows:

- We determine the detection rate of Ly α in our fainter galaxies to be $0.40^{+0.30}_{-0.25}$, compared to $1.00^{+0.00}_{-0.44}$ for the luminous sample of RB16 selected in identical fashion. The rest-frame EWs of our detections are 16–17 Å, marking some of the weakest Ly α detections yet at these redshifts, and we place

strong (3 σ) upper limits of 6–9 Å on the rest of our sources.

- We find simulations of Ly α detection rates in a mostly neutral medium are able to match the observed fainter sample detection rate with a rest-frame $\text{EW}_{0,\text{Ly}\alpha}$ distribution characterized by “normal” galaxies selected with or without an IRAC-excess, while we are unlikely to reproduce the detection rate of their luminous counterparts even with the most extreme EW distribution, suggesting boosted Ly α emission in the latter sample.
- A comparison of galaxy properties from photoionization models shows the UV fainter sample is potentially governed by less extreme properties and reduced ionizing capabilities compared to their bright counterparts.

In this study we confirm the special nature of luminous, IRAC-excess galaxies by investigating whether their faint counterparts – who are less subject to clustering and environmental effects – also display enhanced transmission of Ly α in a predominantly neutral medium.

The contrasting detection rates and photometric properties found here suggest the more extreme systems of UV bright galaxies are able to produce and emit larger amounts of Ly α photons and more efficiently carve out large, early ionized bubbles. However, whether the primary cause of this is their enhanced ionizing properties or the collective ionizing output from neighboring galaxies remains an open question. The arrival of *JWST* and its unprecedented spectroscopic and photometric capabilities will provide the required measurements of emission line diagnostics (e.g., rest-frame UV lines such as Ly α , [C III], He II, and C IV, as well as rest-frame optical lines such as [O III] $\lambda 5007$ Å and H β) as well as confirmations of clustered environments. In addition, the expected confirmation of both existing and new $z > 7$ samples from the telescope will add statistical robustness to the interpretations presented here, and settle the extent to which luminous IRAC-excess objects drive an early reionization.

ACKNOWLEDGMENTS

GRB and TT acknowledge financial support from NASA through grants JWST-ERS-1342 and HST-GO-13459. CAM acknowledges support by the VILLUM FONDEN under grant 37459 and the Danish National Research Foundation through grant DNRF140. RSE acknowledges financial support from European Research Council Advanced Grant FP7/669253. NL acknowledges support from the Kavli fundation. MB acknowledges support by the Slovenian national research agency ARRS through grant N1-0238.

GRB extends his thanks to Rychard Bouwens for providing the photometry of the samples, as well as Joe Hennawi, Debora Pelliccia, and Caitlin Casey for their help with the `PypeIt` software. Additional thanks are extended to Adam Carnall for useful discussions regarding the interpretation of the `Bagpipes` modelling.

REFERENCES

Barone-Nugent, R. L., Trenti, M., Wyithe, J. S. B., et al. 2014, *ApJ*, 793, 17, doi: 10.1088/0004-637X/793/1/17

Bolan, P., Lemaux, B. C., Mason, C., et al. 2021, arXiv e-prints, arXiv:2111.14912. <https://arxiv.org/abs/2111.14912>

Bouwens, R. J., Illingworth, G. D., Oesch, P. A., et al. 2015, *ApJ*, 803, 34, doi: 10.1088/0004-637X/803/1/34

Carnall, A. C., McLure, R. J., Dunlop, J. S., & Davé, R. 2018, *MNRAS*, 480, 4379, doi: 10.1093/mnras/sty2169

De Barros, S., Pentericci, L., Vanzella, E., et al. 2017, *A&A*, 608, A123, doi: 10.1051/0004-6361/201731476

Endsley, R., Stark, D. P., Charlot, S., et al. 2021, *MNRAS*, 502, 6044, doi: 10.1093/mnras/stab432

Fontana, A., Vanzella, E., Pentericci, L., et al. 2010, *ApJL*, 725, L205, doi: 10.1088/2041-8205/725/2/L205

Fuller, S., Lemaux, B. C., Bradač, M., et al. 2020, *ApJ*, 896, 156, doi: 10.3847/1538-4357/ab959f

Gehrels, N. 1986, *ApJ*, 303, 336, doi: 10.1086/164079

Harikane, Y., Ono, Y., Ouchi, M., et al. 2022, *ApJS*, 259, 20, doi: 10.3847/1538-4365/ac3dfc

Hashimoto, T., Laporte, N., Mawatari, K., et al. 2018, *Nature*, 557, 392, doi: 10.1038/s41586-018-0117-z

Hoag, A., Bradač, M., Huang, K., et al. 2019, *ApJ*, 878, 12, doi: 10.3847/1538-4357/ab1de7

Laporte, N., Meyer, R. A., Ellis, R. S., et al. 2021, *MNRAS*, 505, 3336, doi: 10.1093/mnras/stab1239

Laporte, N., Nakajima, K., Ellis, R. S., et al. 2017a, *ApJ*, 851, 40, doi: 10.3847/1538-4357/aa96a8

Laporte, N., Ellis, R. S., Boone, F., et al. 2017b, *ApJL*, 837, L21, doi: 10.3847/2041-8213/aa62aa

Larson, R. L., Finkelstein, S. L., Hutchison, T. A., et al. 2022, *ApJ*, 930, 104, doi: 10.3847/1538-4357/ac5dbd

Leonova, E., Oesch, P. A., Qin, Y., et al. 2021, arXiv e-prints, arXiv:2112.07675. <https://arxiv.org/abs/2112.07675>

Mainali, R., Zitrin, A., Stark, D. P., et al. 2018, *MNRAS*, 479, 1180, doi: 10.1093/mnras/sty1640

Mason, C. A., Naidu, R. P., Tacchella, S., & Leja, J. 2019a, *MNRAS*, 489, 2669, doi: 10.1093/mnras/stz2291

Mason, C. A., Trenti, M., & Treu, T. 2015, *ApJ*, 813, 21, doi: 10.1088/0004-637X/813/1/21

Mason, C. A., Treu, T., Dijkstra, M., et al. 2018a, *ApJ*, 856, 2, doi: 10.3847/1538-4357/aab0a7

Mason, C. A., Treu, T., de Barros, S., et al. 2018b, *ApJL*, 857, L11, doi: 10.3847/2041-8213/aabbab

Mason, C. A., Fontana, A., Treu, T., et al. 2019b, *MNRAS*, 485, 3947, doi: 10.1093/mnras/stz632

McGreer, I. D., Mesinger, A., & D'Odorico, V. 2015, *MNRAS*, 447, 499, doi: 10.1093/mnras/stu2449

McLean, I. S., Steidel, C. C., Epps, H. W., et al. 2012, in Society of Photo-Optical Instrumentation Engineers (SPIE) Conference Series, Vol. 8446, Ground-based and Airborne Instrumentation for Astronomy IV, ed. I. S. McLean, S. K. Ramsay, & H. Takami, 84460J, doi: 10.1117/12.924794

McLeod, D. J., McLure, R. J., & Dunlop, J. S. 2016, *MNRAS*, 459, 3812, doi: 10.1093/mnras/stw904

Mesinger, A., Greig, B., & Sobacchi, E. 2016, MNRAS, 459, 2342, doi: 10.1093/mnras/stw831

Naidu, R. P., Tacchella, S., Mason, C. A., et al. 2020, ApJ, 892, 109, doi: 10.3847/1538-4357/ab7cc9

Oesch, P. A., Bouwens, R. J., Illingworth, G. D., Labb  , I., & Stefanon, M. 2018, ApJ, 855, 105, doi: 10.3847/1538-4357/aab03f

Oesch, P. A., Bouwens, R. J., Illingworth, G. D., et al. 2014, ApJ, 786, 108, doi: 10.1088/0004-637X/786/2/108

Oesch, P. A., van Dokkum, P. G., Illingworth, G. D., et al. 2015, ApJL, 804, L30, doi: 10.1088/2041-8205/804/2/L30

Oke, J. B., & Gunn, J. E. 1983, ApJ, 266, 713, doi: 10.1086/160817

Pentericci, L., Fontana, A., Vanzella, E., et al. 2011, ApJ, 743, 132, doi: 10.1088/0004-637X/743/2/132

Planck Collaboration, Aghanim, N., Akrami, Y., et al. 2020, A&A, 641, A6, doi: 10.1051/0004-6361/201833910

Prochaska, J. X., Hennawi, J. F., Westfall, K. B., et al. 2020, Journal of Open Source Software, 5, 2308, doi: 10.21105/joss.02308

Prochaska, J. X., Hennawi, J., Cooke, R., et al. 2020, pypeit/PypeIt: Release 1.0.0, v1.0.0, Zenodo, doi: 10.5281/zenodo.3743493

Qin, Y., Mesinger, A., Bosman, S. E. I., & Viel, M. 2021, MNRAS, 506, 2390, doi: 10.1093/mnras/stab1833

Qin, Y., Wyithe, J. S. B., Oesch, P. A., et al. 2022, MNRAS, 510, 3858, doi: 10.1093/mnras/stab3733

Qiu, Y., Wyithe, J. S. B., Oesch, P. A., et al. 2018, MNRAS, 481, 4885, doi: 10.1093/mnras/sty2633

Roberts-Borsani, G., Morishita, T., Treu, T., Leethochawalit, N., & Trenti, M. 2022, ApJ, 927, 236, doi: 10.3847/1538-4357/ac4803

Roberts-Borsani, G., Treu, T., Mason, C., et al. 2021, ApJ, 910, 86, doi: 10.3847/1538-4357/abe45b

Roberts-Borsani, G. W., Ellis, R. S., & Laporte, N. 2020, MNRAS, 497, 3440, doi: 10.1093/mnras/staa2085

Roberts-Borsani, G. W., Bouwens, R. J., Oesch, P. A., et al. 2016, ApJ, 823, 143, doi: 10.3847/0004-637X/823/2/143

Robertson, B. E. 2021, arXiv e-prints, arXiv:2110.13160. <https://arxiv.org/abs/2110.13160>

Robertson, B. E., Ellis, R. S., Furlanetto, S. R., & Dunlop, J. S. 2015, ApJL, 802, L19, doi: 10.1088/2041-8205/802/2/L19

Schenker, M. A., Ellis, R. S., Konidaris, N. P., & Stark, D. P. 2014, ApJ, 795, 20, doi: 10.1088/0004-637X/795/1/20

Stark, D. P., Ellis, R. S., Charlot, S., et al. 2017, MNRAS, 464, 469, doi: 10.1093/mnras/stw2233

Strait, V., Brada  , M., Coe, D., et al. 2020, ApJ, 888, 124, doi: 10.3847/1538-4357/ab5daf

Tilvi, V., Malhotra, S., Rhoads, J. E., et al. 2020, ApJL, 891, L10, doi: 10.3847/2041-8213/ab75ec

Treu, T., Schmidt, K. B., Trenti, M., Bradley, L. D., & Stiavelli, M. 2013, ApJL, 775, L29, doi: 10.1088/2041-8205/775/1/L29

Zitrin, A., Labb  , I., Belli, S., et al. 2015, ApJL, 810, L12, doi: 10.1088/2041-8205/810/1/L12

ID	RA [J2000]	DEC [J2000]	H_{160} [AB]	[3.6]-[4.5] [AB]	z_{phot}	$z_{Ly\alpha}$	$f(Ly\alpha)$ [$\times 10^{-18}$ erg s $^{-1}$ cm $^{-2}$]	FWHM [Å]	$EW_{0,Ly\alpha}$ [Å]	Mask ID	iTTime [s]
GSWY-2249353259	03:32:24.93	-27:53:26.04	25.85 \pm 0.13	0.57 \pm 0.25	8.12 \pm 0.36	—	<0.18(3 σ)	—	<6(3 σ)	Mask1	22546
GSDY-2209651370	03:32:20.96	-27:51:37.06	26.14 \pm 0.12	1.05 \pm 0.28	7.94 \pm 0.21	7.962	2.39 \pm 0.83	12 \pm 3	17 \pm 6	Mask1	22546
GNDY-7048017191	12:37:04.81	+62:17:18.98	26.16 \pm 0.07	1.10 \pm 0.20	7.78 \pm 0.25	—	<0.15(3 σ)	—	<6(3 σ)	Mask2	42587
GNWY-7379420231	12:37:37.94	+62:20:22.82	26.50 \pm 0.19	0.46 \pm 0.44	8.21 \pm 0.42	7.108	1.50 \pm 0.71	3 \pm 1	16 \pm 8	Mask2	42587
GNWZ-7455218088	12:37:45.52	+62:18:08.87	26.44 \pm 0.21	0.70 \pm 0.28	7.21 \pm 0.39	—	<0.24(3 σ)	—	<9(3 σ)	Mask2	42587
EGSY8p ^[1]	14:20:08.50	+52:53:26.60	25.26 \pm 0.09	0.76 \pm 0.14	—	8.683	17.0 \pm 7.5	11 \pm 8	28 \pm 13	—	—
EGS-zs8-1 ^[2]	14:20:34.89	+53:00:15.35	25.03 \pm 0.05	0.53 \pm 0.09	—	7.730	17.0 \pm 3.0	13 \pm 3	21 \pm 4	—	—
EGS-zs8-2 ^[3]	14:20:12.09	+53:00:26.97	25.12 \pm 0.05	0.97 \pm 0.18	—	7.477	7.4 \pm 1.0	—	9 \pm 1	—	—
COSY ^[3]	10:00:23.76	+02:20:37.00	25.06 \pm 0.06	1.03 \pm 0.15	—	7.154	25.0 \pm 4.0	—	28 \pm 4	—	—

Table 1. The spectro-photometric properties of our sample of intrinsically fainter Keck/MOSFIRE targets (top half) and their extremely luminous counterparts (bottom half) used in this study. The emission line properties in the top half refer to our Ly α detections and are corrected for instrumental broadening but not for IGM effects. Both sets of galaxies were identified by RB16 on account of their especially red *Spitzer*/IRAC colors and apparent brightness. All photometry is taken from RB16, while the Ly α properties in the lower half of the table come from other analyses. References: [1] Zitrin et al. (2015); [2] Oesch et al. (2015); [3] Stark et al. (2017).

ID	M_{UV} [mag]	β	$\log \text{sSFR}$ [yr^{-1}]	Stellar Age [Myrs]	A_{v} [mag]	Z [Z_{\odot}]	$\log U$
GSWY-224933259	-21.25 ± 0.10	-1.98 ± 0.30	-8.01 ± 0.11	323.68 ± 173.10	0.79 ± 0.21	1.33 ± 0.49	-1.97 ± 0.64
GSDY-2209651370	-21.01 ± 0.07	-2.81 ± 0.20	-8.00 ± 0.06	323.54 ± 168.99	0.27 ± 0.12	0.61 ± 0.40	-1.53 ± 0.41
GNDY-7048017191	-20.73 ± 0.05	-1.60 ± 0.23	-8.00 ± 0.06	397.49 ± 190.27	1.24 ± 0.17	0.93 ± 0.40	-1.54 ± 0.42
GNWY-7379420231	-20.28 ± 0.16	-1.85 ± 0.29	-8.00 ± 0.11	356.57 ± 198.51	0.93 ± 0.30	1.22 ± 0.52	-2.52 ± 0.80
GNWZ-7455218088	-20.56 ± 0.18	-2.09 ± 0.31	-8.01 ± 0.11	391.60 ± 192.69	0.76 ± 0.23	0.80 ± 0.46	-2.05 ± 0.67

Table 2. Galaxy properties as derived from SED-fitting of deep rest-frame UV and optical photometry with *Bagpipes* and a composite star formation history.